Segmentations of hyperspectral imagery: techniques and applications

Jerry Silverman*[a] and Stanley R. Rotman**[a,b]
[a]Air Force Research Laboratory, Hanscom AFB; [b]Ben-Gurion Univ. of the Negev

ABSTRACT

Several approaches for segmenting hyperspectral data and automatically detecting unusual objects in natural scenes are discussed. We demonstrate segmentations of hyperspectral imagery based on of the most significant principal components of the hyperspectral data cube. Several applications of the segmented data are treated. Digital morphological operations can be used to isolate segments that match target criteria. Alternatively, background segments can be used to define background endmembers; pixels that are quantitatively spectrally different from the background can then be designated. Analog morphological operations can then be used for clutter rejection and for the detection of objects of particular size and shape.

Keywords: hyperspectral data, clustering, segmentation, morphological operations

1. INTRODUCTION

Imaging for military, industrial and scientific applications has undergone tremendous changes in recent years. Beside the gradual improvements in image resolution, the use of multi-frequency data has increased[1]. We now regularly gather hyperspectral data containing hundreds of spectral bands. Cameras have been developed for use in the visible, Shortwave Infrared (SWIR), Midwave Infrared (MWIR) and Longwave Infrared (LWIR)[2].

Hyperspectral imaging promises greatly enhanced capability to detect targets. It is well known that the segmentation stage of any automatic target recognition algorithm on standard two-dimensional images is one of the most difficult and important steps[3] and segmentation of hyperspectral imagery is likely to be a key initial step in many procedures for anomaly/ target cueing or detection[4]. A poor segmentation will almost always foil an attempt to find the target. When extended to hyperspectral data, effective segmentation followed by anomaly/target detection becomes even more difficult. The data is inherently three-dimensional with a spectral axis complementing the two spatial dimensions. The problem becomes even more daunting when we realize that the hyperspectral signature of a potential target can be dependent on the time of day, temperature, atmospheric conditions, etc.. Techniques that depend on prior knowledge of the background signatures (or endmembers) are not always feasible. We believe that the most viable approach is to find objects of the right shape and size that are different than the standard background. In this paper, we consider such a process.

The paper is organized as follows. We review a previously presented algorithm that segments hyperspectral images on the basis of the two- or three-dimensional histograms of their principal components[5]. Some modifications to improve our previous approach are mentioned but are detailed elsewhere at this meeting[6]. After exploring the application of morphology directly to the segmented (digital) images, we focus on the processing of our segmented images in tandem with the original hyperspectral data which produces an "anomaly gray-scale image". Such images, when subject to morphological filtering, prove to be powerful anomaly/target cueing algorithms.

*jerry.silverman@hanscom.af.mil; phone 781 377-3295; fax 781 377-4814; Sensor Directorate, Air Force Research Laboratory, AFRL/SNHI 80 Scott Rd. Hanscom AFB, MA USA 01731. **srotman@ee.bgu.ac.il; phone +972-8-6413539; fax +972-8-6472949; Ben-Gurion University, Dept. of Elec. Eng., P.O.Box 653 Beer-Sheva, 84105 ISRAEL.

Infrared Technology and Applications XXVIII, Bjørn F. Andresen, Gabor F. Fulop, Marija Strojnik, Editors, Proceedings of SPIE Vol. 4820 (2003) © 2003 SPIE · 0277/786X/03/$15.00

2. 2D AND 3D HISTOGRAM-BASED SEGMENTATION

The process of spectrally clustering pixels, which forms the basis for classifying hyperspectral data[7], is closely linked to segmenting the image because of the spectral/spatial correlation of natural scenes. On the other hand, a powerful classical approach to segmenting single gray-scale images is by means of the extrema of their histograms[8]. In effect, our segmentations techniques[5] combine the above approaches. We form the histograms from image compressions of the hyperspectral data where the image values are similar for spectrally close pixels. Of the several ways to do this[5], we prefer a segmentation algorithm based on the use of the principal components (PC) of the hyperspectral datacube. (We will describe the method for two components, although the technique is easily extended to 3 or more dimensions.) A two-dimensional histogram is produced from typically the first two components. Peaks (local maxima) in the histogram are located and labeled from 1 to N. The histogram space is then templated to N levels by calculating the distance of any point in the histogram from each peak: that point is then labeled with the label of the "closest" peak. Each pixel in the data cube is then assigned the digital label of its corresponding point in the two-dimensional histogram and segmentation is accomplished.

Some refinements on the above process are described in detail elsewhere[6] and briefly summarized here as follows:

1. The "closest peak" in the above scheme is no longer Euclidian but the peak influences in each dimension are modeled by Gaussian parameters estimated from the co-occurrence histograms of the individual PC's. In effect, this weights the influence of each component separately.
2. In order to generate our histograms, we need to map the PC floating point values into integer bins. The number of segmented levels (up to a point) increases with the chosen number of integer bins leading from coarse to finer segmentations. We developed an interactive form of the algorithm where the user specifies a desired number of segmentation levels and an entropy measure is used to guide a non-linear histogram mapping[9] into that final set of integer bins that achieves roughly the desired number of levels.

Our segmentation techniques have been tested on visible, SWIR, MWIR, and LWIR data and generate excellent results over many scenes. Here, we give three examples in three different bands. The visible hyperspectral image used in Fig. 1 was taken with an AFRL/Solid State Scientific Corporation chromotomographic hyperspectral imaging sensor (CTHIS). The camera design, performance and signal processing characteristics have been described previously[2]. Figure 1 shows segmentations of 12 levels and 6 levels as well as the first two PC's which generated the 2D histogram leading to the segmentations.

The MWIR hyperspectral image of our next example (Figure 2) was taken also with an in-house imaging spectrometer. The imager used is the next generation of the prototype described in earlier work[10]. Again, our histogram segmentations, 9 and 14 levels, are based on the first two PC. (One can get very different segmentations here depending on the parameter used in the non-linear mapping into integer bins[5]. The entropy guide mentioned acts to achieve a better balance between number of segmentation levels given to high and low spatial frequency regions.)

Our final example is extracted from a HYDICE image in the SWIR provided by Spectral Information Technology Application Center (SITAC). HYDICE is a pushbroom imaging spectrometer with 210 spectral bands, which cover the full 0.4 to 2.5 micron spectral range.[7] The size of our extracted image is 238 by 256 pixels and was taken over the CART/ARM Site Lamont. The segmentation to 13 levels is based on a 3D histogram from the first, third and fourth PC's shown. For clarity, we show this result in color; about 5 levels differentiate the panels.

Fig. 1a: First principal component of visible hyperspectral image.

Fig. 1b: Second principal component of visible hyperspectral image.

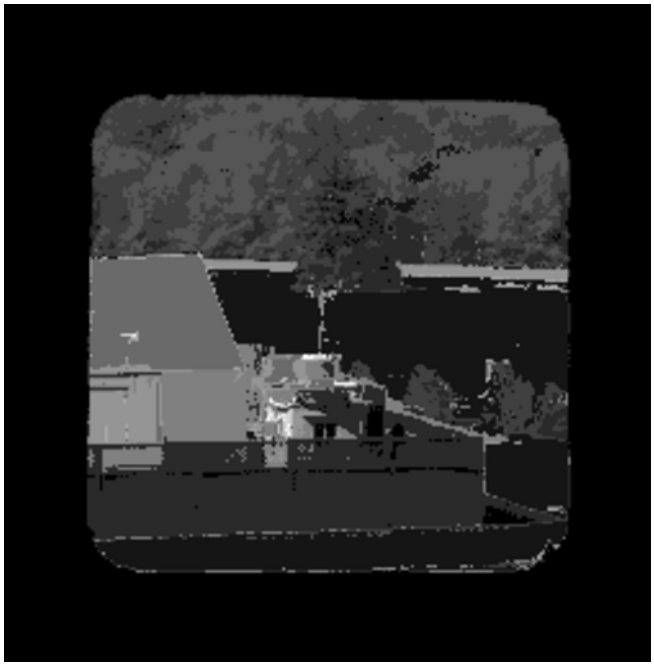

Fig. 1c: 12 level segmentation of visible hyperspectral image.

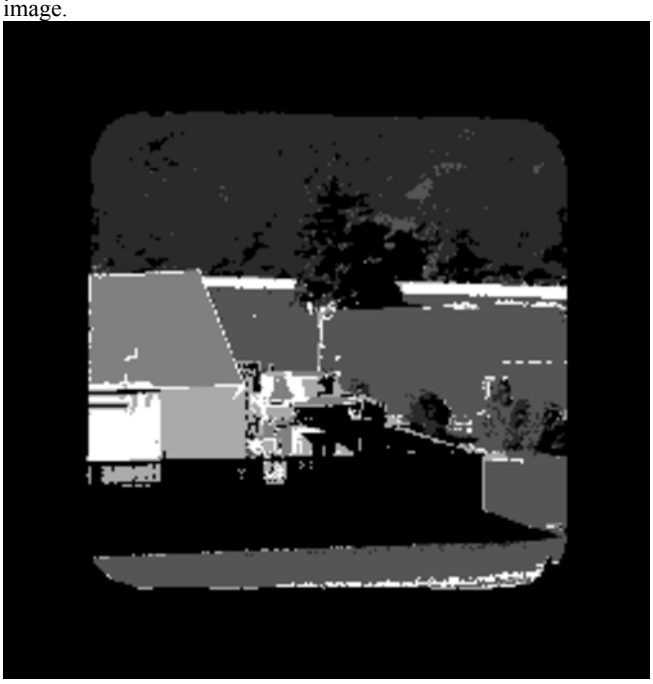

Fig. 1d: 6 level segmentation of visible hyperspectral image.

Fig. 2a: First principal component of MWIR hyperspectral image.

Fig. 2b: Second principal component of MWIR hyperspectral image.

Fig. 2c: 9 level segmentation of MWIR hyperspectral image

Fig. 2d: 14 level segmentation of MWIR hyperspectral image.

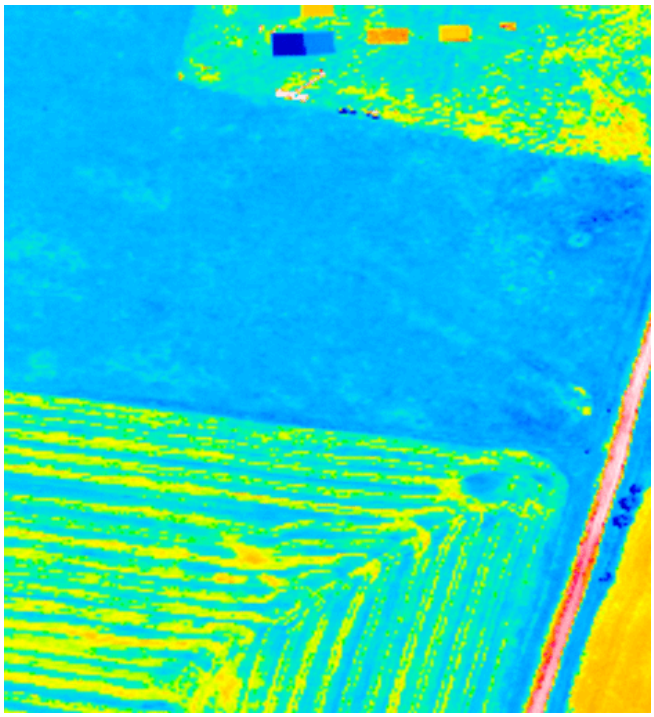

Fig. 3a: First principal component of HYDICE hyperspectral image.

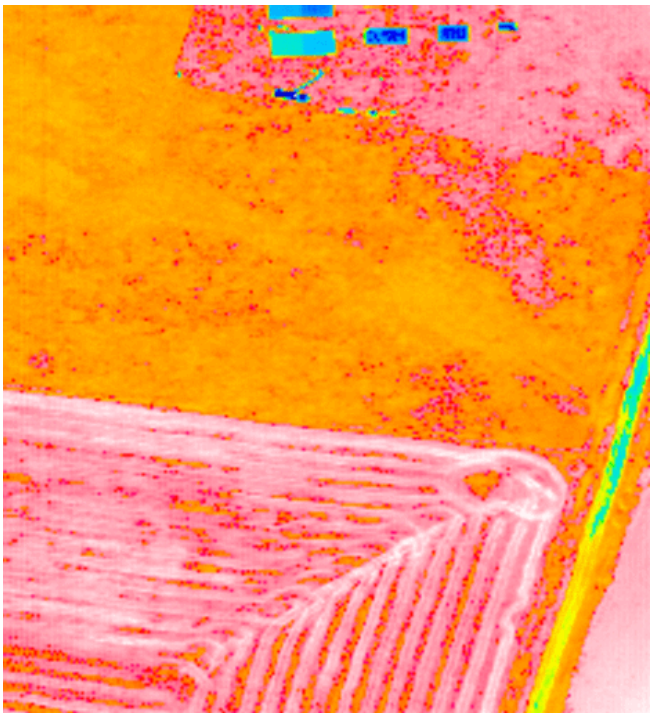

Fig. 3b: Third principal component of HYDICE hyperspectral image.

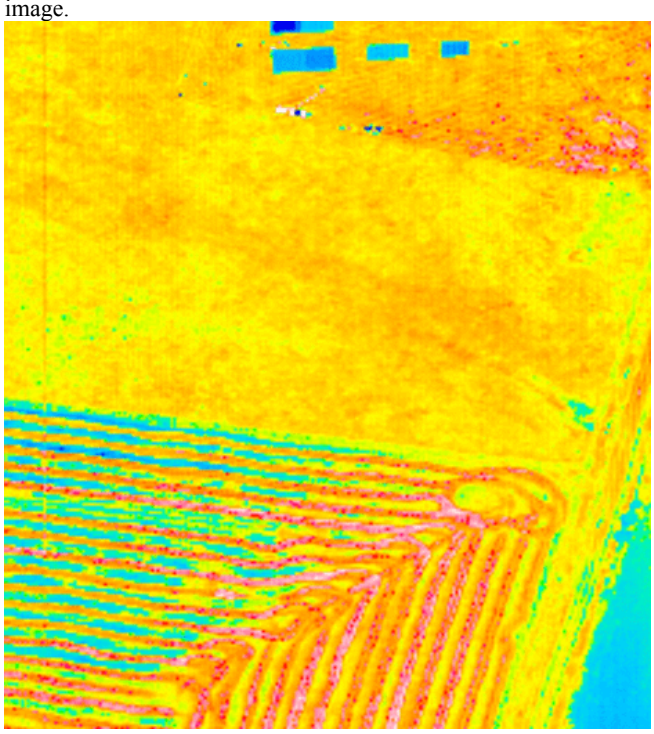

Fig. 3c: Fourth principal component of HYDICE hyperspectral image.

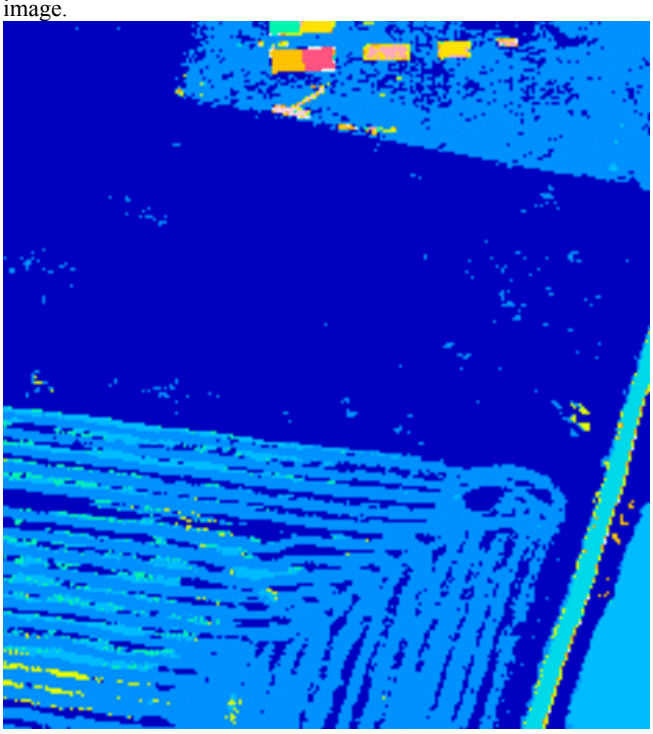

Fig. 1d: 13 level segmentation of HYDICE hyperspectral image.

3. APPLICATIONS

3.1 Introduction

We are aware of at least four uses of segmented Hyperspectral images:

1. Application of regional constraints in improving computed tomographic data reconstructions[11]
2. Preliminary classification
3. Operator display
4. Target cueing/detection.

Here we concentrate on the last application and contrast two broad approaches to utilizing segmentations in target cueing/detection.

For this purpose and in order to introduce a more quantitative approach than achieved by purely anecdotal examples, we base this section on four HYDICE data cubes taken of the (roughly) same scene at the ARM_site over three days in June, 1997 at 4:30, 5:30, 5:37, and 12:20 pm respectively. Scenes 1, 2 and 4 were taken at about 6000 ft. and scene 3 at about 5000 ft. The scene content is similar but simpler than that used in Figure 3 and consists of ploughed farmland, a road , a triangular shaped region of trees, and three panels (taken as the targets).

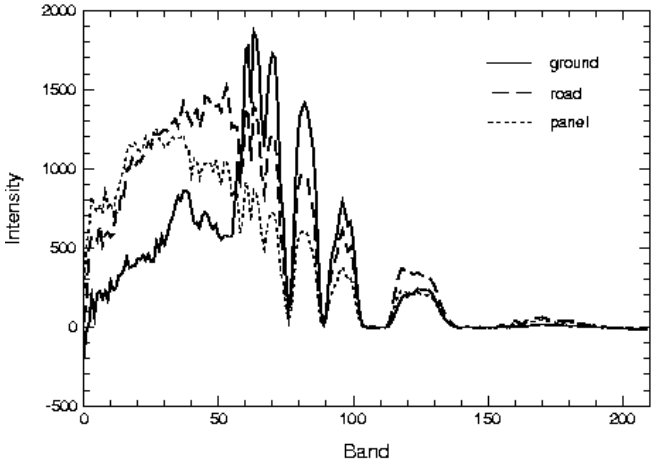

Fig. 4a: Sample signatures from HYDICE image.

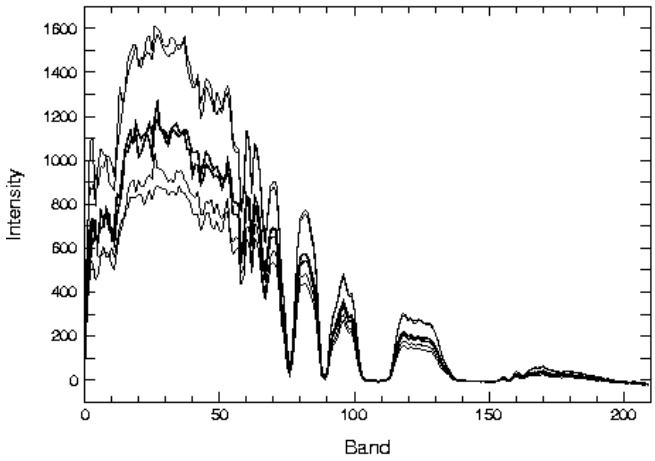

Fig. 4b: Sample pairs of signatures from 3 panels of the HYDICE image.

Figure 4a shows typical profiles of a panel, road and ground pixel, while 4b shows three pairs of panel pixel profiles. The almost matching pairs are from the same panel and exemplifies that for all scenes the main distinction between panels is a scaling constant. Figure 5 shows segmentations to 6, 5, 8, and 5 levels of the 4 scenes respectively. Note that many of the panels segment almost fully to one digital level but some, like the upper panel in Fig. 4b or the panels in Fig. 4c, are hybrids of two digital levels. This has significant consequences for the approaches to be discussed.

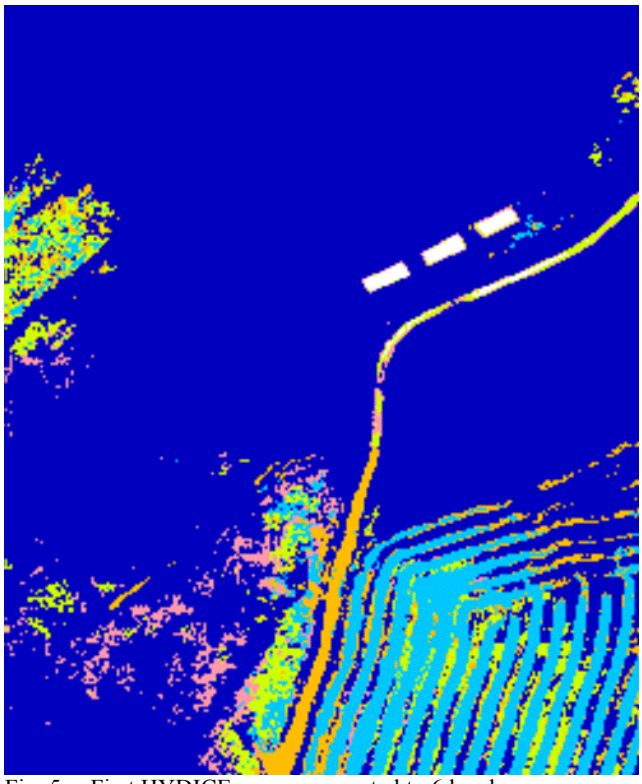

Fig. 5a: First HYDICE scene segmented to 6 levels.

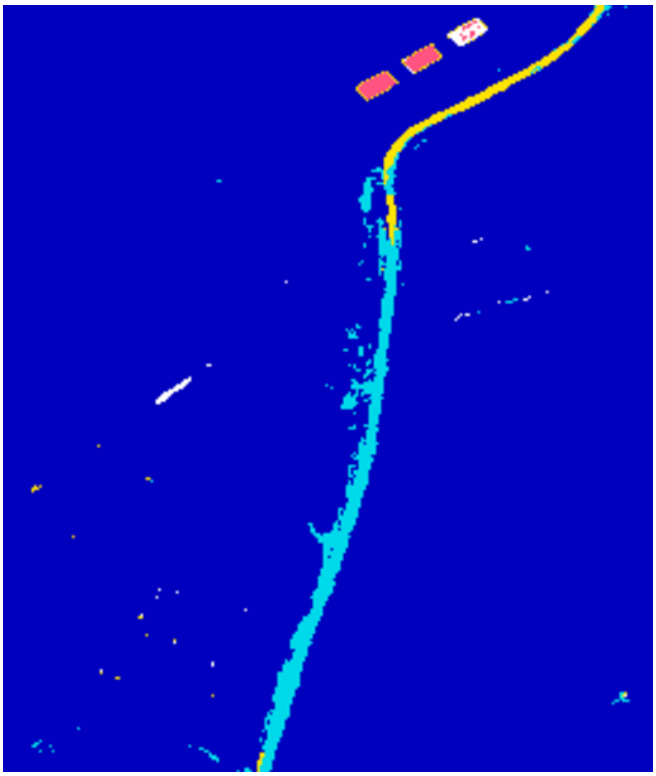

Fig. 5b: Second HYDICE scene segmented to 5 levels.

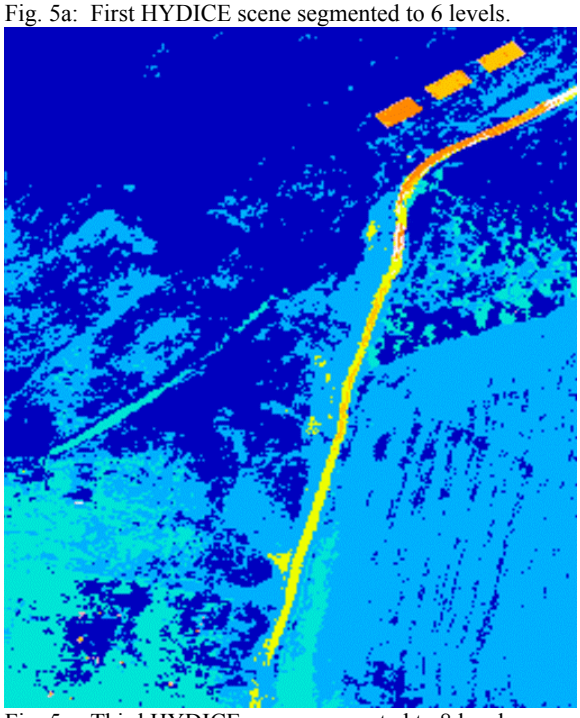

Fig. 5c: Third HYDICE scene segmented to 8 levels.

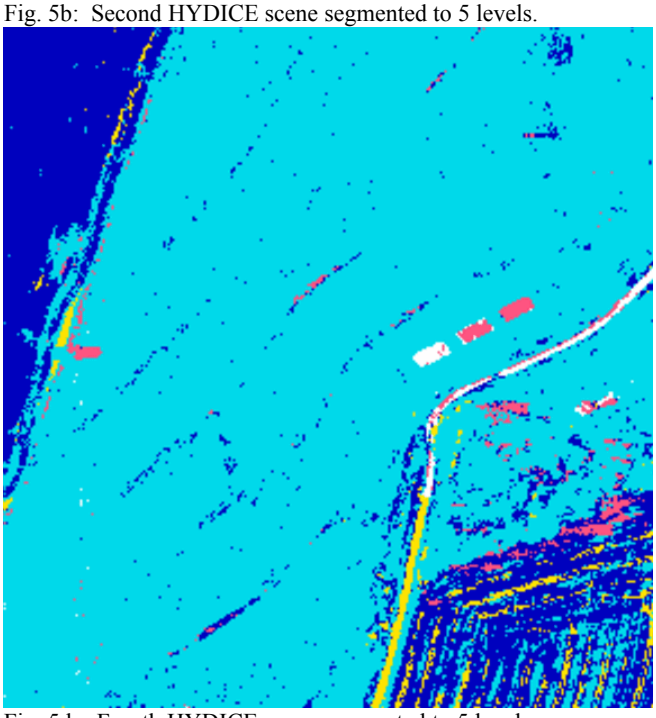

Fig. 5d: Fourth HYDICE scene segmented to 5 levels.

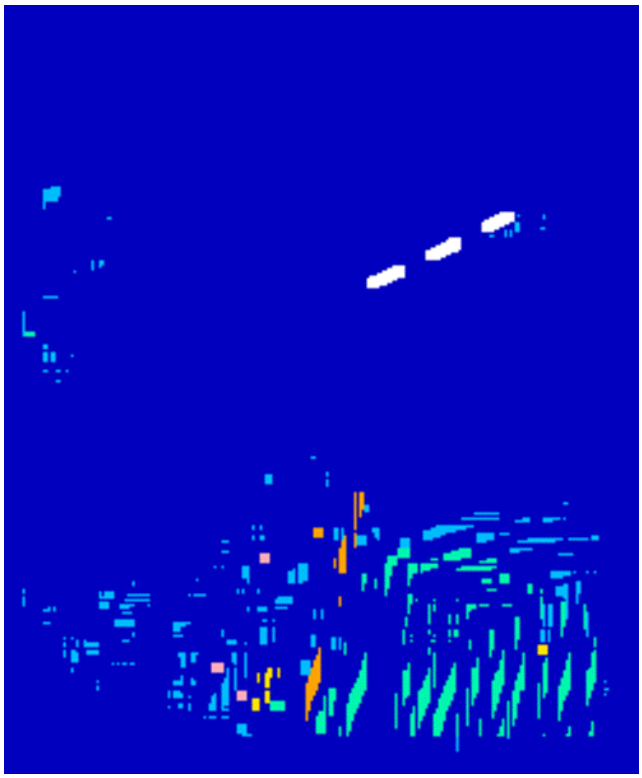

Fig. 6a: Morphological results of Scene 1

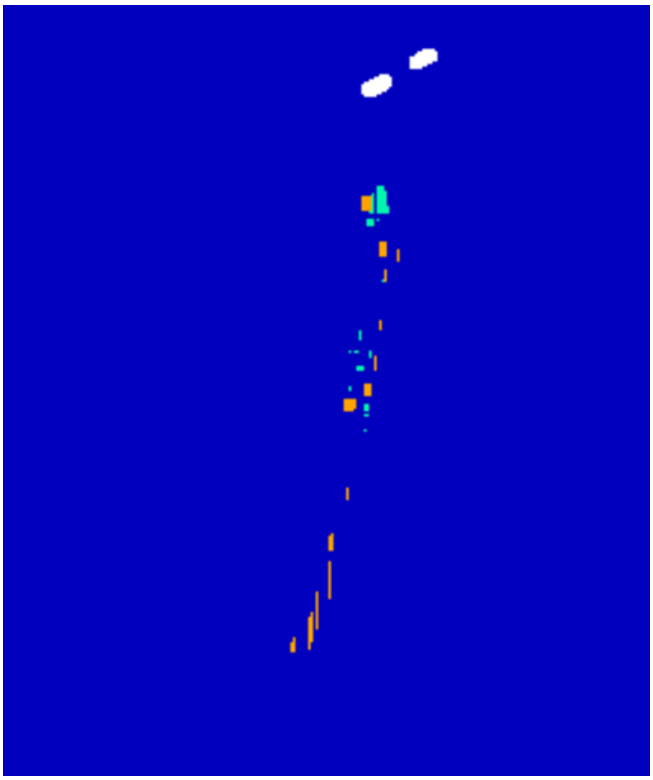

Fig. 6b: Morphological results of Scene 2

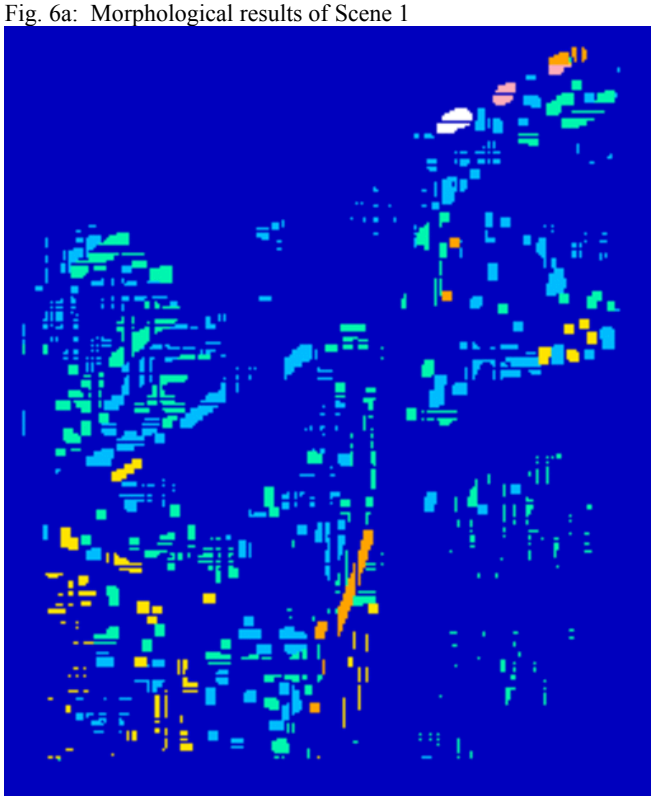

Fig. 6c: Morphological results of Scene 3

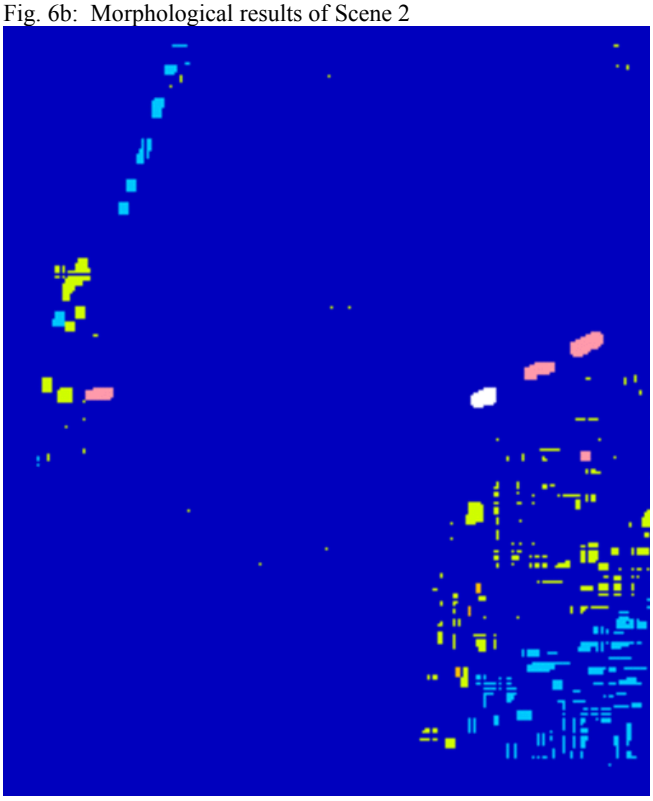

Fig. 6d: Morphological results of Scene 4

3.2 Direct use of (digital) segmentations

For clarity, we should specify that by the term segment, we refer to all the pixels in a segmentation labeled with the same digital value. For example in scene 4 (Fig. 5d), the "white" segment (digital level 5) forms the bulk of the lowest panel but many of the road pixels have the same segmentation level. We use the term "*segmented cluster*" for a spatially contiguous region, such as the upper panel in scene 4, segmented to the same value, regardless if there are pixels elsewhere designated with this same value.

The simplest approach is to apply size and shape criteria, i.e. morphological operations, directly to the segmentations and extract desired *segmented clusters*. For this purpose, we have explored combinations of openings and white hats[12] rectangular alignments or diagonal alignments. To improve on the realism of our results, we assume here and in the following section that our knowledge of the target is confined to its maximum and minimum dimensions with unknown orientation. For the panels in these scenes, we choose 4 and 16 pixels for the extreme dimensions and apply the following rectangular morphological operations: a 4 by 4 opening and pairs of 1 by 16 and 16 by 1 white hats (original image minus opening). By appropriate fusion of these three operations, we retain *segmented clusters* that fit within a minimum window size of 4 by 4 and a maximum size of 15 by 15 pixels.

The results of these morphological operations applied to the segmentations of Fig. 5 are shown in Figure 6 and reveal the problems with this approach. If the panels form *segmented clusters* as in Fig. 5a and 5d, one recovers the panels almost in toto (Fig. 6a and 6d). Problems are created by hybrid panel segmentations that result in the absence of panel 3 in Fig. 6b and the recovery of just fragments of the panels in 6c. A further problem is the lack of any magnitude differentiations in the recovered *segmented clusters* in Fig. 6. Clearly, further operator intervention such as cross checking back to the original data cube would be needed to weed out the false alarms.

The approach treated in the next section, which postpones the morphological operations until after an anomaly detection stage, ameliorates these problems.

3.3 Use of anomaly images

As shown above, the direct use of the segmented image to detect targets is dependent on the proper segmentation of the targets from the background. When the target is composed of different types of materials or temperatures that are not compatible with each other, this is often not possible. For example, a hot running tank will often have a hot spot for the engine with a cold chassis. These may well segment into two or more *segmented clusters*. In addition, parts of the target may be included by mistake into background segments. Both of these results will lead to difficult if not impossible target detection if based on the digital segmentations.

To circumvent these problems, we start with a few basic assumptions:

1. The targets only occupy a small percentage of the overall image.
2. The average signatures of the background segments accurately portray the signatures of the background pixels and are distinct from the signatures of the targets.

With these assumptions, we construct an anomaly detector to assist in our target detection work. We segment the image, as described above, and rank the *segmented clusters* by their size. We assume that some large percent X of the pixels in the image constitutes background; X is typically 90 – 98% of the picture. We then consider the largest *segmented cluster*; if it by itself consists of X% of the background, then this segment by itself defines the background. If it does not, then we add the next *segmented cluster* in size. We continue until we reach X% of the image. When this is done, we have a number of segments defined as background (including all the pixels with the same digital values as the chosen *segmented clusters*); the other segments are defined as candidate target groups.

The pixels comprising each segment can be averaged together from the original hyperspectral datacube to form an average pixel signature for that segment. (Note that we are referring to the signatures obtained in the original data and not to the principal components data; subtleties in the original data can be characteristic of the "target" which are not immediately apparent in the principal component domain.) Thus, the segments that comprise the background can be

characterized by a set of average hyperspectral vectors derived from these segments. Similarly, the potential targets can be characterized by the average signatures of the (100 – X)% segments which remain in the image.

Figure 7a shows again (reduced scale) our segmentation of scene 1 along with the result of the background cueing process (7b) just described. Digital segments labeled 1, 2 and 4 (ground, ploughed areas, and road portion) form the three background segments and constitute 93% of the image. The candidate 7% remaining target pixels are shown in blue. To generate an anomaly detector, we now take each pixel in the image and compare it to the average background signatures.

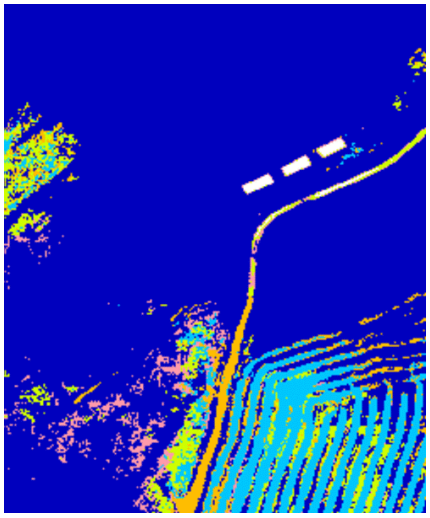

Fig. 7a: Segmented results of Scene 1

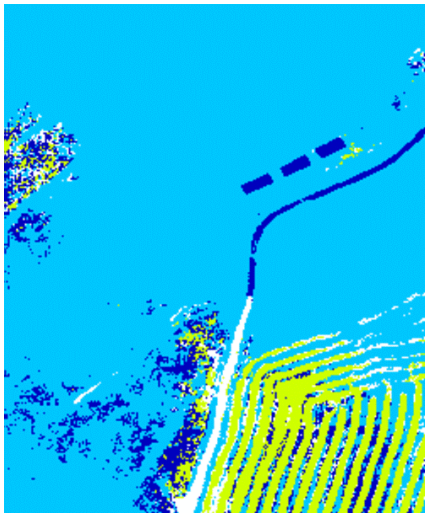

Fig. 7b: Background cueing result for scene 1; potential targets are in deep blue.

Fig. 7c: Anomaly image of Scene 1 based on Euclidian measure

Fig. 7d: Anomaly image of Scene 1 based on Angular metric

Fig. 7e: Morphological result from Fig. 7c

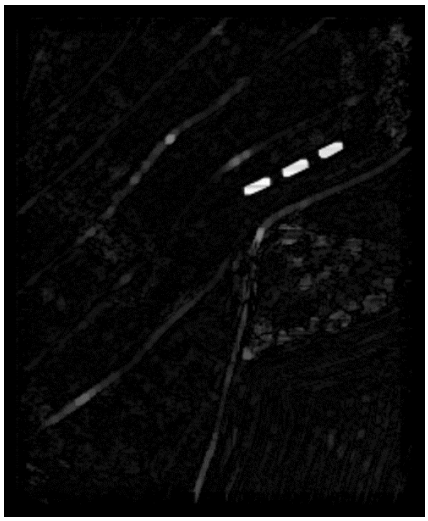

Fig. 7f: Morphological result from Fig. 7d

Two metrics have been tested for this comparison; in one we take the Euclidean distance between the pixel and the average signature; in the second, we evaluate the spectral angle that the pixel makes to the average signature in the N dimensional space. For each metric, the value assigned to the pixel is the minimum value of the metric obtained with respect to any of the background signatures. In this anomaly-detecting stage, pixels with high metric values will be those which don't fit into the background.

Figure 7c and 7d show a linear display of the two anomaly images (Euclidian and angular measures). We next apply the same morphological operations detailed above to these gray-scale anomaly images. (Note that in the digital domain, each digital level is treated as a separate black/white image in the morphological process; while in the gray-scale domain, the morphology is applied to the single analogue image. Hence adjacent regions can interfere and modulate each other in the analogue mode.) The results in 7e and 7f show the panels as well above the remaining pixels.

We show the full corresponding results for scene 4 (the most challenging of the scenes) in Figure 8. Here two segments of ground pixels constitute 96.4% of the background and segments 3,4 and 5 (blue in Fig. 8b) are the target candidate pixels. Since the panels in this case are closer in magnitude to the background pixels than are other candidate target pixels, the Euclidian measure of anomaly fails (8c) but the angular measure still affords excellent results (8d and 8f).

In Figure 9, we also show partial results on scenes 2 and 3 for the angular measure. The results are equally good. For scene 3, 9c and 9d, the outer morphological dimension was increased to 18 pixels to accommodate the larger fringerprint; we note some self interference in this case.

3.4 Final Comments

The approach in the last section of generating an anomaly image cued by the segmented image appears to be a very powerful and robust technique. Consider the following cases that may have occurred at the background-cueing stage of this technique. 1. The target (e.g. the panel) is part of the (100-X)% of the target pixels and represents a *segmented cluster* in the original segmentation. 2. The target is also part of the (100-X)% of the pixels but is not a *segmented cluster* in the original segmentation but is a hybrid of non-background levels. 3. Portions of the target are segmented with the same levels as background segments. 4. The target was one of the chosen *segmented clusters* taken as constituting background. (Note that we try to avoid this last possibility by not allowing X to approach too close to 100%.)

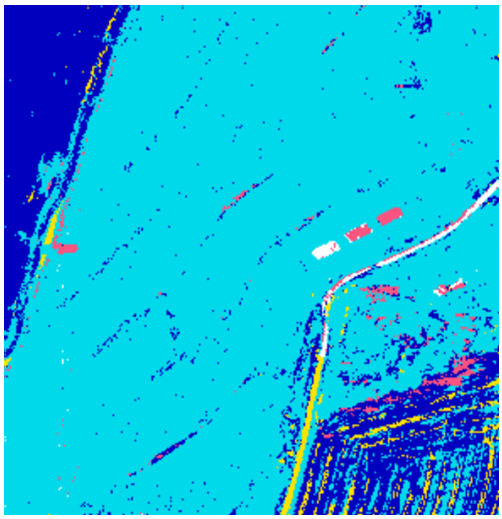

Fig. 8a: Segmented results of Scene 4

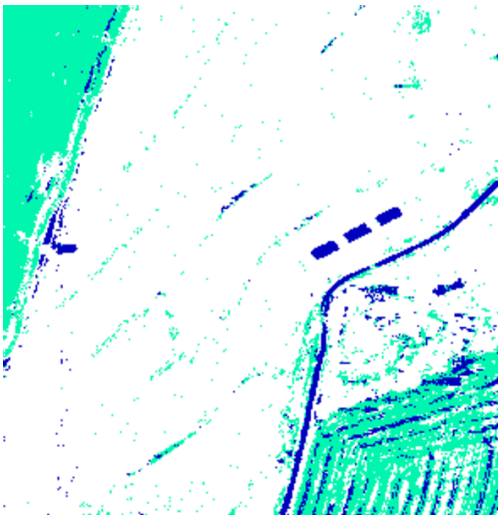

Fig. 8b: Background cueing image of Scene 4

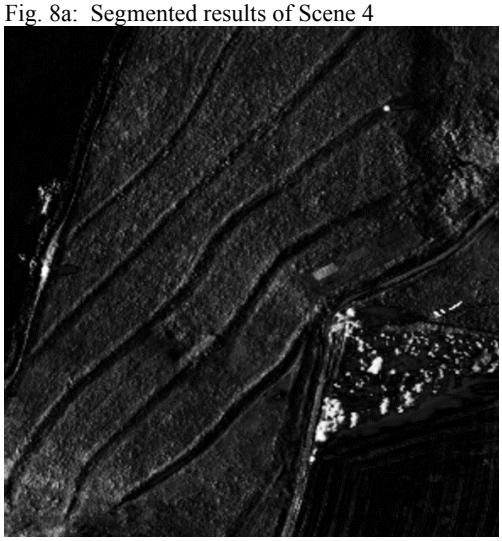

Fig. 8c: Anomaly image of Scene 4 based on Euclidian measure

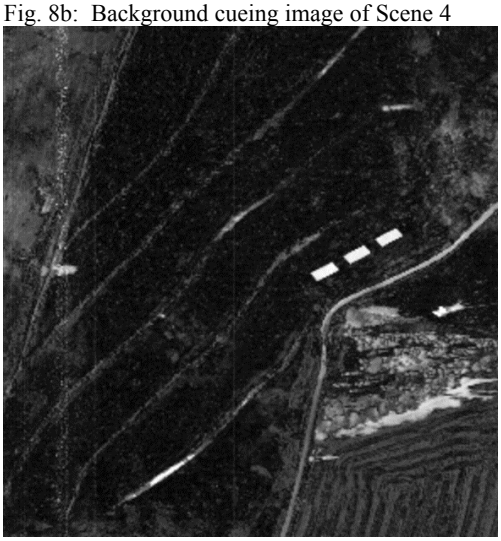

Fig. 8d: Anomaly image of Scene 4 based on Angular metric

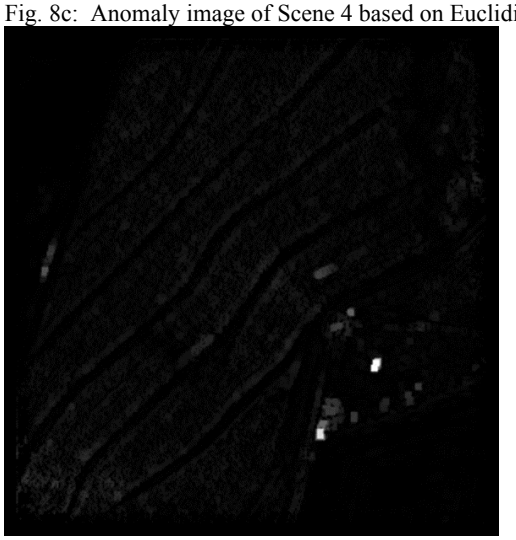

Fig. 8e: Morphological result from Fig. 8c

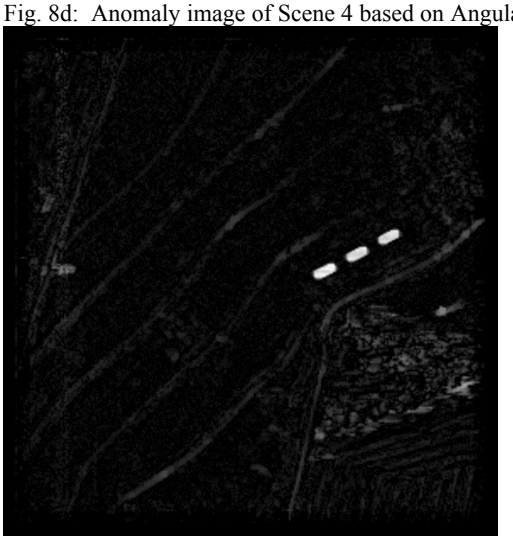

Fig. 8f: Morphological result from Fig. 8d

Fig. 9a: Anomaly image of Scene 2 based on Angular metric.

Fig. 9b: Morphological result from Fig.9a.

Fig. 9c: Anomaly image of Scene 3 based on Angular metric.

Fig. 9d: Morphological result from Fig.9c.

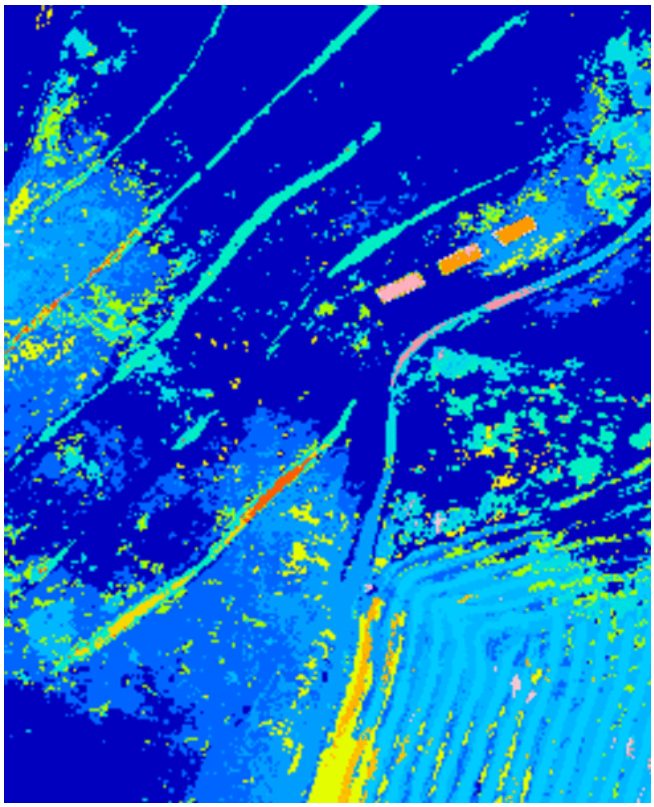

Fig. 10a: Scene 1 segmented to 19 levels

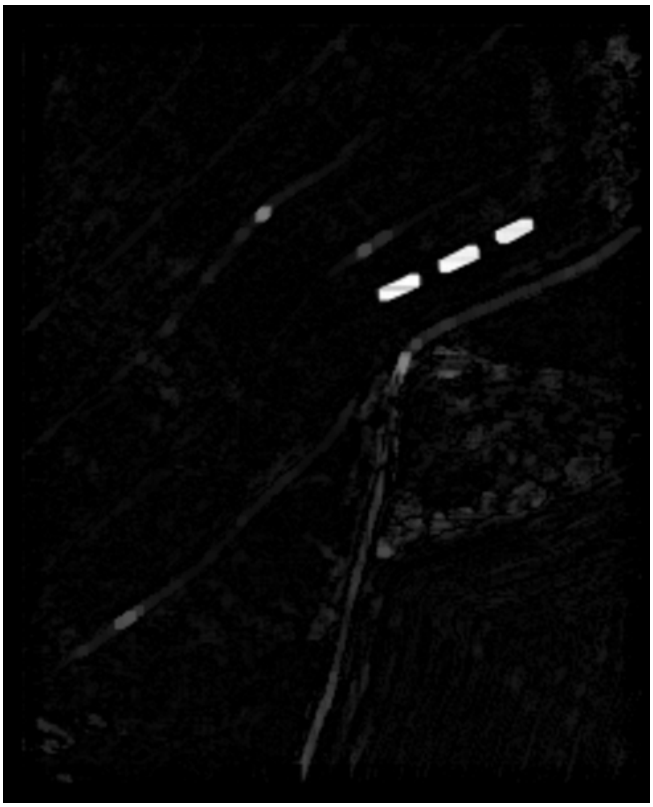

Fig. 10b: Morphological results of Fig. 10a.

Of the four cases, the first is clearly optimal. In that case, the target should be detectable by the segmenting and morphological procedures described in Section 3.2, as well as in our anomaly detecting process of 3.3. The other three cases are likely to fail for the direct digital morphological method, while cases 2 and 3 are still quite viable for the anomaly approach. For case 2, the target pixels have not influenced the background average pixel signatures and one can detect these pixels as being distinct from the background. As for case 3, if the background pixel levels are much greater in number than the target pixels similarly labeled, then the particular features of the target pixels that distinguish them from the background may not enter the average background signature and anomaly detection will still work. Only in the fourth case, where the target entered the background as its own *segmented cluster* does one expect difficulty in detecting the target.

As one indication of this expected robustness, we resegment the first scene to 19 levels as shown in Fig. 10a. The panels segment largely to two levels and direct application of morphology loses the middle panel and increases as well the number of false alarm fragments (not shown). Our background cue image (also not shown) has the first 9 levels, 98% of the pixels, taken as background. Application of the morphology to the angular-measure anomaly image gives the excellent result in Fig. 10b, very similar to that shown in Fig. 7f.

3. CONCLUSIONS AND FUTURE WORK

We have presented in this paper several approaches towards developing an automatic segmentation and target acquisition system based on the use of hyperspectral imagery. An initial segmentation of the datacube is achieved by clustering the pixels into groups with similar values in the first few principal components images and working with the corresponding 2 or 3D histograms. This segmentation can be used directly with digital morphological operations to select objects similar to the target. In addition, average background endmembers are derived from the segmented

images; each pixel in the image is then evaluated based on its similarity to the background signatures, either with a Euclidian or angular anomaly metric. Morphological operations can again be applied either to the analog results of the anomaly image to highlight areas of non-conformity with the background. Considerable testing should be conducted to determine the ruggedness of this method.

One avenue for additional research involves the anomaly detection approach. Algorithms (e.g., the Orthogonal Subspace Projection) have been developed by Chang et al.[13] to pick out the components of sample vectors that are orthogonal to a subspace defined by a set of background endmembers. By coupling our method of generating background endmembers to these techniques and by then matching the results to target vectors, we should be able to develop more sophisticated metrics for classifying the pixels in our image.

Our initial testing on Hydice images gives us reason to hope that our segmentation and anomaly detection methods may apply generally for many applications in other hyperspectral spectral regimes. In particular, we are interested in studying the information content in infrared MWIR and LWIR data and the exploitation of hyperspectral sensors to detect targets in these images. Since the MWIR data contains information both from the reflectivity of the objects as well as the material emissivity, its information content should be quite high with a large potential for exploitation with hyperspectral techniques. Overall, the work presented in this paper points to several possible avenues of research in this rich field.

ACKNOWLEDGMENTS

The cameras used to collect the visible and MWIR data were designed and fabricated by William Ewing, Toby Reeves and Steven DiSalvo of our laboratory. The HYDICE data was provided by the Spectral Information Technology Application Center (SITAC). We are grateful to our Linda Bouthillette for graphic assistance. This work was carried out under Air Force Task 2305BN00. We'd like to acknowledge partial support of the Paul Ivanier Center for Robotics and Industrial Production, Beer-Sheva, Israel. This work was performed while one of the authors (SRR) held a National Research Council Research Associateship Award at the Air Force Research Laboratory at Hanscom AFB.

REFERENCES

1. J.A. Richards and J. Xiuping, *Remote Sensing Digital Image Analysis: An Introduction*, Springer-Verlag, Berlin, 1999.
2. J.E. Murguia, T.D. Reeves, J.M. Mooney, W.S. Ewing, F.D. Shepherd, and A.K. Brodzik, "A compact visible/near infrared hyperspectral imager", Proc. SPIE 4028, 457-468 (2000). See also Ref. 1, 7 and 10.
3. R. C. Gonzalez and R.E. Woods, *Digital Image Processing*, Addison Wesley, Reading, MA (1993).
4. D.W. Paglieroni and D.E. Perkins, " Automatic extraction of closed pixel clusters for target cueing in hyperspectral images", in *Signal and Data Processing of Small Targets 2001*, Oliver E. Drummond, Editor, Proceedings of SPIE Vol. 4473, 51-61 (2001).
5. J. Silverman, C. E. Caefer, J.M. Mooney, M.M. Weeks, and P. Yip, "An automated clustering/segmentation of hyperspectral images based on histogram thresholding", in *Imaging Spectrometry VII*, Michael R. Descour, Sylvia S. Shen, Editors, Proceedings of SPIE Vol. 4480 65-75 (2002).
6. J. Silverman, S.R. Rotman and C.E. Caefer, "Segmentation of Hyperspectral Images from the Histograms of Principal Components", *in Imaging Spectrometry VIII,* Sylvia S. Shen *,* Editor*,* Proceedings of SPIE Vol. 4816 (2002).
7. R. A. Schowengerdt, "Remote Sensing: Models and Methods for Image Processing", Academic Press, San Diego (1997).
8. F. M. Wahl, *Digital Image Signal Processing*, Chap. 5, Artech House, Boston, 1987.
9. V.E. Vickers, "Plateau equalization algorithm for real-time display of high-quality infrared imagery", *Opt. Eng.* **35(7)**, pp. 1921-1926 (1996).
10. J. M. Mooney, V. E. Vickers, M. An, and A.K. Brodzik, "High throughput hyperspectral infrared camera", *J. Opt. Soc. Am. A,* **14(11)**, pp. 2951-2961 (1997).
11. J.M. Mooney, Private communication.

12. J.-F. Rivest and R. Fontin, "Detection of dim targets in digital infrared imagery by morphological image processing", Opt. Eng. **35(7)**, pp. 1886-1893 (1996).
13. C.-I. Chan and H. Ren, "An Experiment-based quantitative and comparative analysis of target detection and image classification algorithms for hyperspectral imagery", IEEE Trans. GRS **38(2)**, pp. 1044-1063 (2000) and references therein.